CHARACTERIZING EXPLOSIVE VOLCANIC ERUPTIONS: A PASSIVE MICROWAVE SATELLITE

APPROACH

By

Daniel Lopez

Thesis

Submitted to the Faculty of the

Graduate School of Vanderbilt University

in partial fulfillment of the requirements

for the degree of

MASTER'S OF SCIENCE

in

Earth & Environmental Sciences

May 10th, 2024

Nashville, Tennessee

Approved:

Ralf Bennartz, Ph.D.

Kristen Fauria, Ph.D.

Lin Meng, Ph.D.

ACKNOWLEDGMENTS

TABLE OF CONTENTS

LIST OF TABLES

LIST OF FIGURES

CHAPTER 1

Introduction

Explosive volcanic eruptions are among the most significant devastating natural hazards to occur on Earth, resulting in the endangerment of people, wildlife, and property. During an explosive eruption, a volcano may eject clouds of hot rocks (pyroclasts), volcanic particles (ash), and gases that may form an eruption column or volcanic plume. Besides impacts very close to the vent, the ejected material can rise into the atmosphere, spread at a neutral buoyancy level, and then fall onto surrounding communities. These impacts can be far-reaching with fallout known to occur 100s to 1000s of kms from vents for the largest eruptions, which can disrupt air travel and affect air quality (Wilson et al., 2012). If the ash reaches the stratosphere, volcanic particles can be a source of dramatic changes in global weather/climate patterns by affecting Earth's radiative budget, resulting in observed reductions of diurnal cycles, summer cooling, stratospheric heating, and winter warming (Robock, 2001) (Carn et al., 2016). Estimating the composition of volcanic plume content of eruption clouds is therefore valuable, as it provides insight into the chemical composition, aerosol properties, and gas-to-particle conversion processes that may inform our understanding of short and long term effects on the planet's climate.

Satellite observations of volcanic eruption retrievals of ash began in 1993 (Wen and Rose, 1994) and with a first case study in 1996 exploring passive microwave (PMW) observations (Delene et al., 1996) for volcanic eruptions. Currently, there are various sensors serving the purpose of observing volcanic ash emissions, primarily being infrared, visible and LiDAR (Prata and Lynch, 2019). Infrared sensors can penetrate through clouds to some extent and offer night-time observations but are less effective in differentiating between ash and meteorological clouds, leading to potential misinterpretations in ash concentration. Visible imagery also has the associated disadvantage of only working during daylight hours, restricting its usage. High ice (cirrus) clouds permeate large portions of the Earth, especially the tropics, resulting in obstruction of volcanic plumes underneath in visible and infrared spectral ranges. In comparison, due to the longer wavelength and associated low extinction of microwave radiation, PMW sensors can provide valuable data irrespective of the time of day or presence of clouds (Petty, 2006), providing a potentially clear snapshot of deeper features.

Over the last decades, various space-borne remote sensing instruments have been used to detect and quantify volcanic ash as well as volcanic gases, such as SO_2 from remote sensing observations. Most studies have relied on visible/near-infrared and infrared passive observations as well as on limited observations by space-borne radars or LiDARS. For a detailed overview on remote sensing of volcanic eruptions (see Prata and Lynch (2019)). While in 1996 a first case study explored passive microwave (PMW) observations (see
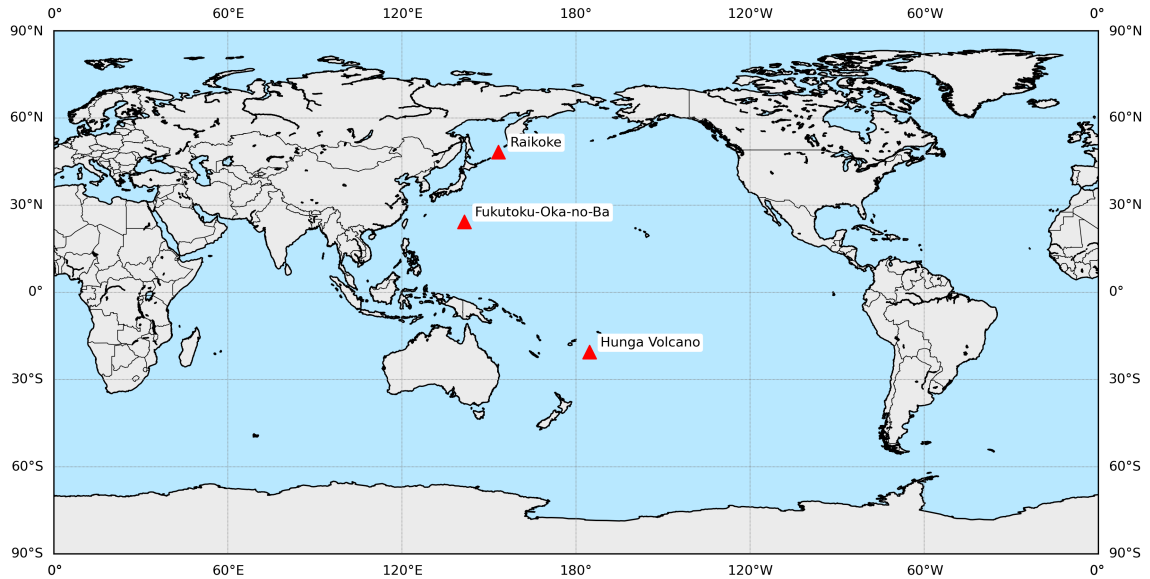
Figure 1.1: The map illustrates the geographical positions of notable volcanic eruptions that have been analyzed in the study. Red triangles mark the exact locations of these events, including Raikoke, Fukutoku-Oka-no-Ba, and Hunga Volcano.

Delene et al. (1996)), in recent years, the use of PMW for volcanic remote gained some limited traction via a set of further case studies (Marzano et al. (2006); Marzano and Coauthors (2018); Montopoli et al. (2014); Montopoli et al. (2013); Romeo et al. (2023)) which showed, despite the low resolution of PMW sensors, the success of PMW retrieval of ash concentrations and ash cloud detection for various volcanic plumes. While the retrieval methods of Montopoli et al. and Marzano et al. depend on ground-based weather radars, and Romeo et al. utilize the Visible Infrared Imaging Radiometer Suite (VIIRS) and Advanced Very High Resolution Radiometer (AVHRR), our objective is to develop a methodology that relies exclusively on PMW satellite data for quantity retrievals. High PMW and submillimeter channels have also shown to be sensitive to volcanic ash (Bryan et al., 2017) in the the 1992 Crater Peak/Spurr eruption, showing potential for future PMW satellite missions for the study of volcanic plumes.

PMW sensors have traditionally been utilized for their insights into precipitation measurements. PMW sensors are capable of retrieving the internal structure and intensity of precipitation events due to their sensitivity to emission of liquid and scattering of frozen hydrometeors, enabling detailed observations of rainfall rates, snowfall, and distributions (Skofronick-Jackson and Johnson, 2002). For volcanic ash, the sensors can detect the scattering of microwave radiation by the ash particles. Two key satellite platforms equipped with advanced PMW sensors are the Global Precipitation Measurement (GPM) and the Special Sensor Microwave Imager/Sounder (SSMIS). The GPM systems satellite mission intention is to improve our understanding of Earth processes related to precipitation and water (Hou et al., 2014). Here, we utilize the data outputs of

GPM Microwave Imager (GMI), which provides dual polarization frequencies at 10-190 GHz. Additionally, SSMIS provides observations of surface, atmospheric, and topographical parameters, including precipitation with frequencies ranging from 19-183 GHz (Grody et al., 2008). Utilizing sensors with both and and low frequencies is useful here, as it allows us to determine the general content of a volcanic plume in terms of its water, ice, and ash content.

In this study, we study analyze recent major explosive over/near ocean eruptions with a volcanic explosivity index (VEI) greater than three using SSMIS and GPM multi-frequency PMW sensors, locations of which are mapped in Figure 1.1, which includes the 2021-2022 Hunga Volcano, the 2021 Fukutoku-Oka-no-Ba, and the 2019 Raikoke eruption. We propose that precipitation-focused PMW spaceborn sensors utilized for analyzing volcanic ash plumes can provide useful information when used in conjunction with other spaceborn sensors, as it could retrieve information along the depth not available to other shallow-retrieving sensors. Specifically, we provide a comprehensive overview and comparison of explosive volcanic eruptions from the perspective of passive microwave satellites and other sensors, empirically analyzing each case in terms of the observed radiances, which is a measure of the energy that is emitted or reflected by the hydrometeors and captured by the satellite sensors.

CHAPTER 2

Methodology

2.1 Dataset Description

	SSMIS					GMI		
Channel	Freq	P	Swath		Channel	Freq	P	Swath
8	150	H	S3		1	10.6	V	S1
9	183±1	H	S3		2	10.6	H	S1
10	183±3	H	S3		3	18.7	V	S1
11	183±7	H	S3		4	18.7	H	S1
12	19	H	S1		5	23	V	S1
13	19	V	S1		6	37	V	S1
14	22	V	S1		7	37	H	S1
15	37	H	S2		8	89	V	S1
16	37	V	S2		9	89	H	S1
17	91	V	S4		10	166	V	S2
18	91	H	S4		11	166	H	S2
					12	183±3	V	S2
					13	183±7	V	S2

Table 2.1: Channel specifications for from GMI-XCAL. The left table denotes the data available from SSMIS16, SSMIS17, and SSMIS18 white the right table denotes data available from GMI.

Passive microwave observation data for this study was retrieved from the Global Precipitation Mission's (GPM) Intercalibration project, which provides intercalibrated brightness temperatures from a series of passive microwave conically scanning instruments. The dataset includes DMSP F-16, F-17,F-18 Special Sensor Microwave Imager Sounder (SSMIS), Advanced Microwave Scanning Radiometer-2 (AMSR-2), and the Global Precipitation Mission Microwave Imager (GMI). For the purpose of our study, we will use GPM as well as SSMIS observations as those sensors cover the frequency range 18–190 GHz, which is needed to fully address the emission and scattering signatures of meteorological clouds and volcanic ash (Petty, 1994a). The full range of frequencies and polarizations available from each satellite in the XCAL dataset are listed in Table 2.1.

In our analysis, we also incorporate data from Himawari-8, a geostationary satellite equipped with the Advanced Himawari Imager (AHI). This satellite uses spectral channels 1 to 4 (0.47 μm, 0.51 μm, 0.64 μm, and 0.86 μm) to generate high-resolution RGB imagery, aiding in the visualization of volcanic plumes during daylight. Additionally, Channel 12 at 10.4 μm is used for infrared observations.

The SSMIS satellites has a spatial resolution of approximately 25 km for lower frequency channels and 15 km for higher frequency channels at nadir, with a temporal resolution of twice-daily coverage. The Global Precipitation Measurement Microwave Imager (GMI) offers spatial resolutions ranging from 10 km to 3 km at nadir, depending on the channel, and covers the entire Earth approximately every 3 hours. The Advanced Himawari Imager (AHI) on Himawari-8 provides spatial resolutions of 0.5 km to 2 km, depending on the channel, with full-disk observations every 10 minutes and more frequent observations possible for targeted regions.

Volcanic data and information related to location, name, date, and eruption strength for this study was taken from the Smithsonian Institution National Museum of Natural History Global Volcanism Program (https://volcano.si.edu/). This database provided a catalog of Holocene and Pleistocene volcanic eruptions, and includes eruptions within the operational timeframe of SSMIS and GPM satellites. The selection criteria of eruptions for this study were based on the eruption's VEI, focusing on those with significant atmospheric impacts and thus more likely to be detectable by the PMW sensors. Here, we choose eruptions with a VEI greater than or equal to three. In the future, we plan to expand our methodology to include smaller eruptions and determine if they can be detected by passive microwave satellites.

2.2   ERA5 Data Integration

To understand the background meteorological conditions during the three eruptions we study, European Centre for Medium-Range Weather Forecasts Reanalysis (ERA5) (Hersbach et al., 2020). Specfically, these renalysis data provides atmospheric state variables corresponding to the times and locations of volcanic eruptions, and is used for simulating background brightness radiances from various satellites and those included within this study (SSMIS and GMI). The integration process involves aligning ERA5 data with observations from the Global Precipitation Measurement (GPM) and Special Sensor Microwave Imager/Sounder (SSMIS) across the frequency and polarization channels detailed in Table 2.1. This ensures that the atmospheric conditions reflected in the ERA-Interim data are consistent with those during the satellite observations to within 3 hours. The ERA5 reanalysis dataset has a global spatial resolution of approximately 31 km (0.28125 degrees) on a regular latitude-longitude grid for its atmospheric parameters. Here, we use ERA5 data as the basis for simulating cloud-free background brightness temperatures near volcanic eruptions for the three eruptions included in this study.

2.3   TIROS Operational Vertical Sounder Radiative Transfer Model Application

The TIROS Operational Vertical Sounder (TOVS) RTTOV is used to simulate clear-sky background brightness temperatures for the GPM Microwave Imager (GMI) and SSMIS channels outlined in Table 2.1 (Hocking

et al. (2019); Saunders and Coauthors (2007); Saunders and Coauthors (2018)). This model employs atmospheric profiles from the ERA5 data to calculate expected brightness temperatures for specific atmospheric conditions. These simulations provide a baseline for comparison with actual satellite observations during volcanic events, allowing us to calculate the difference in brightness temperatures (ΔTB) and isolate the impact of volcanic ash clouds on the microwave radiative signal.

2.4 Eruption Collocation

For each volcanic eruption, given the time and location of eruption, we downloaded each satellite data file for that particular period. Each produced scene was manually visually inspected for thermal anomalies and, if the scene contained a positive visually confirmed eruption during an overpass, it was added to our analysis. We took samples from each satellite referenced before, including GMI, SSMIS16, SSIS17, and SSMIS18. The GMI and SSMIS systems have slightly differing channel frequencies, seen in Table 2.1. Here, we assumed that channels that are close to each other are relatively equivalent (i.e 37 and 36 GHz). Himawari-8 has constant coverage over the volcanic eruptions in this study due to its geostationary orbit, making eruption collocation straightforward with aligning eruption and satellite observation times.

2.5 Physical Basis

Over the ocean, microwave brightness temperatures, which are used in PMW satellites, are sensitive to a combination of several factors, including warm but weakly polarized/unpolarized emission by liquid water, water vapor, oxygen in the atmosphere, cold but strongly polarized emission from the ocean (Petty, 1994a) in low microwave frequencies, and to scattering by precipitation-sized ice particles aloft in high microwave frequencies. Scattering by precipitation-sized ice particles effectively traps warm radiation and reduces the observed brightness temperature at higher frequencies (Bennartz and Bauer (2003); Chen and Bennartz (2020)). This reduction in brightness temperatures at higher frequencies, or the 'scattering signature', is observed for the three volcanic eruptions investigated in this proposal. In this study, frequencies below 37 GHz are considered low frequencies, while those above 37 GHz are categorized as high frequencies (150 GHz is our analyzed high frequency for plotting).

For analyzing the radiative impact of volcanic ash clouds, we employ a differential method comparing observed and simulated cloud-free brightness temperatures (ΔTB) laid out in (Chen and Bennartz, 2020). This difference is defined as:

$$\Delta TB = TB_{obs} - TB_{sim} \tag{2.1}$$

Where the cloud-free simulations will be performed utilizing the RTTOV and ERA5. The global sim-
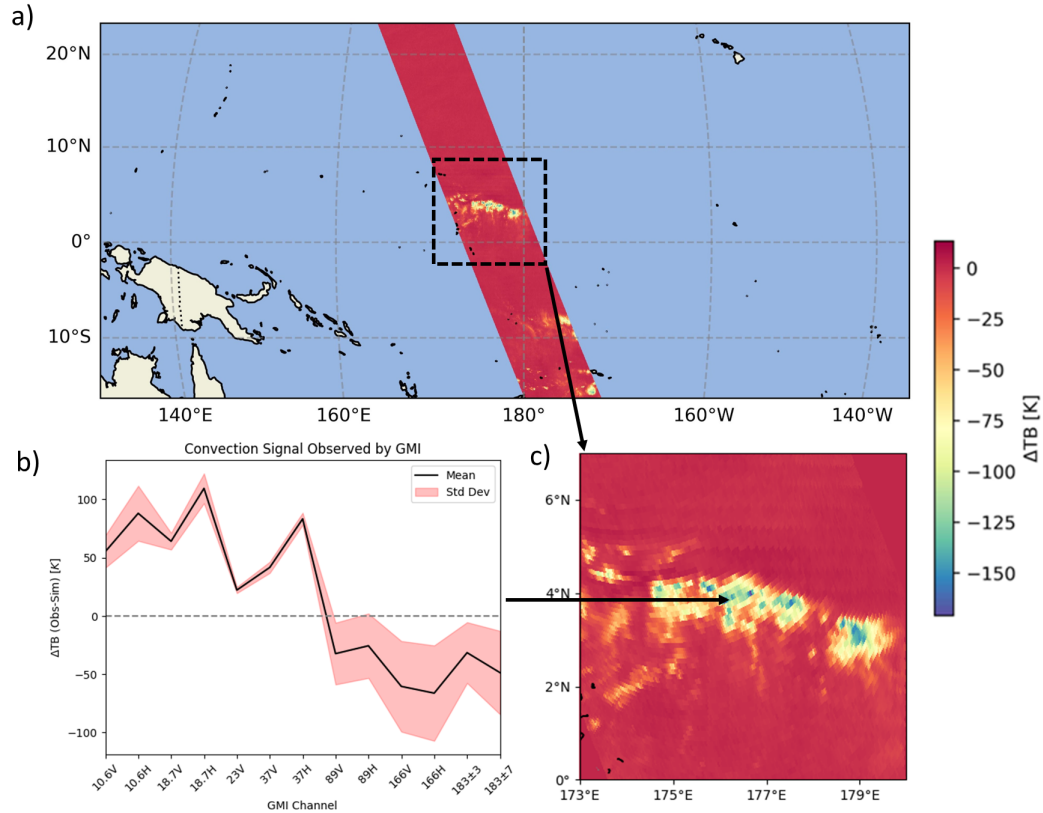
Figure 2.1: Example of a typical meteorological convective cloud. Panel a depicts an area from the Pacific ocean where the example convective sample was taken from, northeast of Australia, the black box denoting the specific bounding box given to panel c. Panel b showcases the mean and standard deviation of ΔTB values sampled across the convective cloud. Panel c depicts PMW observations of typical convective clouds by GMI in 166V GHz from the black box in panel a.

ulations will then be matched in time and space to each individual satellite observation to calculate ΔTB utilizing the Hamburg Ocean Atmosphere Parameters and Fluxes from Satellite Data (HOAPS) software (National Center for Atmospheric Research Staff, 2022).

Here, TB_{obs} denotes the microwave observations, while TB_{sim} represents the simulated clear-sky background brightness temperatures. In ΔTB, emission by liquid water in the atmosphere will appear more strongly in lower microwave frequencies, while scattering by ice and ash particles will appear in higher frequencies in PMW sensors (Petty, 1994b). The complementary nature of emission and scattering at low and high frequencies, respectively, motivated our choice for GPM and SSMIS, as they contain both low and high passive microwave frequencies, as it allows us to distinguish between different types of particles in the atmosphere. However, since the emission signature can only be observed over ocean, we are restricted towards analysis of volcanic ash plumes that extend over ocean. This limitation stems from the distinct microwave emission and scattering characteristics of land surfaces compared to ocean surfaces, which can significantly

alter the TB signals. Since the highest frequency available in this study is 183 GHz, very small particles, such as from cirrus clouds, are invisible (Ekelund et al., 2020).

Convective clouds, especially those with strong vertical structures, present unique microwave signatures. At lower frequencies, emissions from cloud liquid water droplets are the primary signal, with emission intensity rising with increasing water content. At higher frequencies, scattering by ice particles dominates, reducing the observed TB. Such scattering and emission characteristics are effectively quantified by passive microwave (PMW) sensors using ΔTB, as seen in Figure 2.1. In lower frequencies (10.6-37 GHz), we see the difference between observed and simulated radiances exceeding 50 Kelvin. In contrast, the ΔTB for higher channels (89-183 GHz) falls below magnitudes of -30 Kelvin. The use of ΔTB is an important factor in isolating the effects of hydrometeors, both for deep convective clouds and for volcanic ash plumes. It allows the disentanglement of features and their related signal from background signatures, making comparisons between events and the retrieval of the signal's magnitude more straightforward. Additionally, we can make assumptions on what it should look like comparing the meteorological content of an ash plume to a convective cloud (Figure 3.4), when looking at specific channel combinations. Specifically, volcanic eruptions typically exhibit lower emissions and values near zero at low frequencies due to their relatively low water content, while their high ash content results in a scattering signature similar to convection with large negative values at higher frequencies.

Results/Discussion

3.1 Hunga Volcano

The first sample case study focuses on the 2021-2022 Hunga Volcano (HV) eruption, a VEI scale 5 submarine eruption located in the southern Pacific Ocean 65km north of the island Tongatapu. HV began erupting in December 2021, with a massive eruption on January 15th, 2022. This event was considered one of the most significant eruptions in recent history since Mount Pinatubo's eruption in 1991 (Wright et al., 2022). The explosive force produced a plume that reached heights of 55-58 km (Carr et al., 2022), injecting ash and other aerosol particles into the lower stratosphere. Given HV's submarine volcanic nature, it also ejected water from the surrounding ocean into the atmosphere. The PMW data, complemented by infrared (IR) observations in Fig. 3.1, provide a detailed account of the 2021-2022 Hunga Volcano (HV) eruption's evolving radiative signature.

During the first hours of the eruption in the first row of Fig. 3.1, there is not a visible signal retrieved from panel Fig. 3.1a, when the volcanic eruption has not intensified yet, resulting in ΔTB values very near background levels. In Fig. 3.1e, as the frequency increases, the plume of HV becomes more apparent seen by the decrease in temperatures following the emitted ash traveling southwesterly from the location of HV. Panel q tells the same story along all channels - low frequencies (under 36 GHz) have very little changes in ΔTB while high frequencies have a large negative magnitude. During this phase of the eruption, HV is emitting only small quantities of liquid water, which produces only a small emission signal, while still releasing large amounts of ash that generates a scattering signal. The information retrieved from IR and Vis in panels l and m provides more detail of the plume characteristics, where details and ash concentrations are more visible farther away from the vent. In this case, the PMW observations cannot resolve the finer particles with lower concentrations that are further from the central part of the plume.

During one of the volcano's outbursts, denoted in the second row of Fig. 3.1, a larger amount of emission is detected by SSMIS in the lower frequencies as well as increased scattering signatures in the higher frequencies. In Fig. 3.1b, a more visible signal is detected, denoted by slightly cooler ΔTB compared to the background (-5K). In panel r, we see that 19 GHz frequencies as well as 37 GHz has a positive ΔTB of 25K. In panel f/150GHz, the HV plume shows an enhanced level of scattering. Given, that the plume is estimated to have reached 18km (Gupta et al., 2022), the significant amount of ash in addition to the freezing of liquid water results in the increase in negative magnitude of ΔTB in lower frequencies. During this time period of
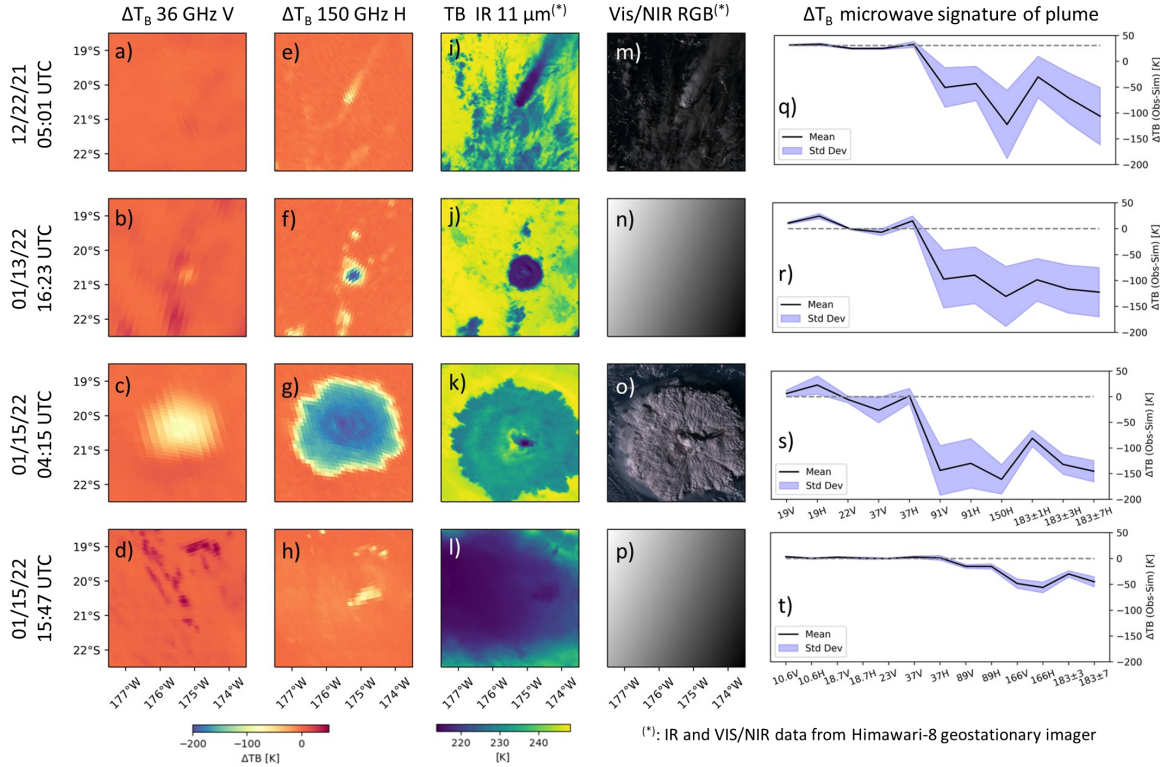
Figure 3.1: Visual time series of the 2021-2022 Hunga Volcano eruption. The first and second column from the left is 36 GHz 150 GHz from PMW observations. The third and fourth column is Infrared and Visible data from Himawari-8. The rightmost column represents a distribution of pixels within the plume of the same row across all available frequencies, where the black line denotes the mean and the blue area denotes the standard deviation.

the eruption, visible imagery is unavailable, which is given by the blank n panel. Comparing panels f to j, the IR data, similar to the initial phase of the eruption, has more detail compared to the PMW observations and shows a larger plume width.

During HV's climactic eruption in the third row of Fig. 3.1, we a much more enhanced scattering signal and an increase of emission in the lower frequencies. Compared to the previous small outburst on January 13th, the January 15th explosion ejected a huge amount of material into the atmosphere - which is reflected by the PMW observations. In Fig. 3.1c, there is a decrease in ΔTB of 40K compared to the background. In Fig. 3.1c, the plume is much smaller in diameter compared to the IR data in panel k and the visible imagery in panel o, where the PMW at this frequency is only retrieving values closer to the central vent of the volcano. In Fig. 3.1g, details of the plume are much more visible, with colder values also closer to the center of the vent providing information of a denser column of the ejected material. During the first three stages of the eruption, the amount of scattering increases as the amount of ejected material increases, with a ΔTB decrease of -50k.

One showcased advantage of PMW sensors is the visualization of characteristics obstructed in the other IR/visible sensor during the latter stages of the HV eruption. In panel h of Fig. 3.1, there is a clear plume extending from the location of the center of the volcano, unobstructed by cirrus shield in panel l. This proves as a significant advantage of the utilization of PMW satellites, where we can retrieve information below thin layers of ash that would be normally partially/completely blocked, such as the start point and plume of a continuously venting HV. After the eruption, ΔTB values shift much more toward the background and decrease in magnitude significantly in panel t.

As mentioned earlier, liquid water emission dominates the signal in the lower frequencies of passive microwave. In panels a,b, and d of Fig. 3.1 exhibits this lack of signal, with ΔTB values near zero. During the climactic eruption in Fig. 3.1c, however, we see a very distinct signal in the 19H and 37V frequencies of SSMIS. This signal is different than what we would expect from a convective cloud, as it lacks the magnitude in the lower channels equivalent to the high amounts of emission of liquid water in a typical cloud. The high-frequency PMW channels (above 89 GHz) demonstrate heightened sensitivity to ice particles within the volcanic plume. The observed cooler temperatures in these channels indicate substantial microwave scattering. As the eruption intensified, evidenced by the observed decrease in ΔTB in panels e, f, g, and h, of Fig. 3.1 the ice nucleation of the water and ice-coated ash as it ascended aloft with the plume led to enhanced scattering effects. Additionally, typical convective cells and precipitating clouds, described by the emission and scattering characteristics above, should show a distinct ΔTB signal compared to volcanic ash, supporting our hypothesis that volcanic columns, compared to a typical atmospheric environment, are sufficiently unique from meteorological columns.

3.2 Fukutoku-Oko-no-Ba

The second case study is of the 2021 eruption of submarine volcano Fukutoku-Oka-no-Ba (FOnB), a VEI scale 4 eruption located in the Bonin Island of Japan 5 km northeast of South Iwo Jima. FOnB's plume is estimated to have reached up to 16 km in the atmosphere (Maeno et al., 2022). This eruption was characterized by the discharge of large volumes of ash and gas, as well as the formation of a new island due to the accumulation of volcanic material. In contrast to HV significant ash content, FOnB is characterized by a liquid water and ice dominated plume (Fauria et al., 2023). The PMW data is again complemented by infrared (IR) observations provided in Fig. 3.2.

Similar to HV, FOnB is a submarine volcano with access to large amounts of water in the Pacific Ocean that has the potential to eject upwards. Similar to HV in the before and after stages of the eruption, there is little difference in signal of the plume compared to the background signature in panels a,b, and c supported by m,n, and o of Fig. 3.2. In 37H, there is an increase in magnitude of 10 Kelvin compared to the background,
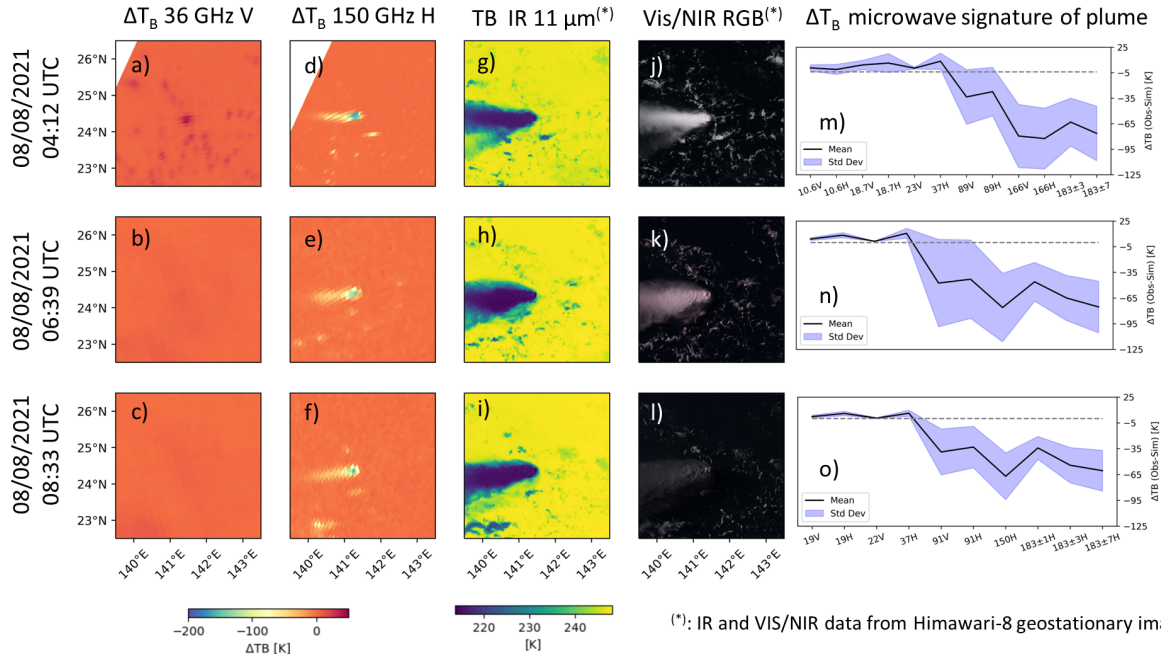
Figure 3.2: Visual time series of the 2021 eruption of Fukutoku-Oka-no-Ba.

suggesting there there was more water content producing an emission signal in the earlier stages of the eruption compared to the latter stages. The spread of ΔTB values across the plume in panels m, n, and o of Fig. 3.2 are all similar to HV panel in Fig. 3.1. There is a peak in 19H of approximately 7 Kelvin in the FOnB eruption, compared to a peak of 25 Kelvin in HV. The emission signal is relatively lower, indicating a lower concentration of particles for FOnB, matching the lesser explosivity level. At these lower frequencies, FOnB exhibits significant amounts of liquid water, yet the quantity is still much lower compared to that in convective clouds.

The higher frequencies (above 89 GHz) are very similar and characteristic of the eruption in HV. In panels d, e, and f, of Fig. 3.2, we can visually see the core of the volcanic plume, a feature not visible in the infrared and visible. We can see that this core is much colder than the surrounding plume, indicating an increased amount of scattering from ice particles in the higher frequencies. The rest of plume, however, is invisible from the PMW perspective. These particles near the edge are likely too small for detection and are small nucleated ice particles, indicated by the low infrared temperature. In the spread of ΔTB values in m,n and o, the profile is again similar to that of HV with a lower mangitude of approximately 80 kelvin, indicating a distinct pattern of the scattering signal from the output of volcanic eruptons.

For FOnB, there is a lack of PMW overpasses before and after the eruption. We remark this as a downside of utilizing passive satellites with relatively low refresh rates as a tool of observation for quick events such as volcanic eruptions. Yet, PMW observations here provides information not available to the IR or visible,
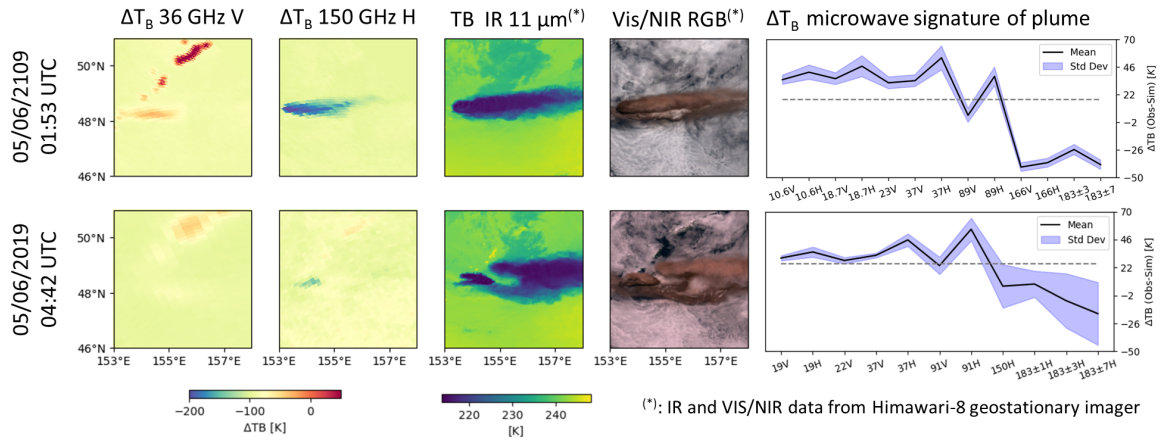
Figure 3.3: Visual time series of the 2019 Raikoke volcanic eruption.

including an estimation of the width of the core of the plume at different stages of the eruption.

3.3 Raikoke

The Raikoke Volcano, located on the Kuril Islands in Russia, underwent a significant eruption in June 2019. The eruption began on June 22nd, 2019, with a series of explosive activities that propelled ash and gas up to 13 kilometers into the stratosphere. The eruption's plume was observed to spread extensively across the North Pacific, restricting air travel and posed hazards to aviation. The Raikoke eruption was particularly significant due to its sulfur dioxide (SO_2) emissions, which were the highest recorded for a volcanic eruption in the 21st century (de Leeuw et al., 2021). For the purpose of this study, Raikoke is an interesting case because of the high mixing between the plume and meteorological clouds, adding an additional complexity to our analysis. During the initial phase of the eruption in Fig. 3.3 first row, we see an intact plume extending eastward into the Pacific Ocean. As the eruption progresses and weakens in the bottom row, the plume begins to break up and mix heavily with the surrounding clouds.

In the lower frequencies of Raikoke in Fig. 3.3, we see that in panel a that the plume, in contrast to the previous two eruptions, is warmer than the background ΔTB values by approximately 30 kelvin in the first row. This indicates that each pixel column of the atmosphere in the Raikoke eruptions contains a much stronger emission signal from the inclusion of meteorological clouds, which contain more liquid water at lower levels. The magnitude is less than that of a meteorological cloud referenced in Fig. 2.1, due to the clouds being non-convective and containing less liquid water. As the plume breaks up in panel b, the lower frequency ΔTB magnitude lessens about 20 Kelvin, likely owing to the lack of clouds over the plume vent during this time period.

For the higher frequencies, there is a drastic shift in the middle frequencies of around 89 GHz compared
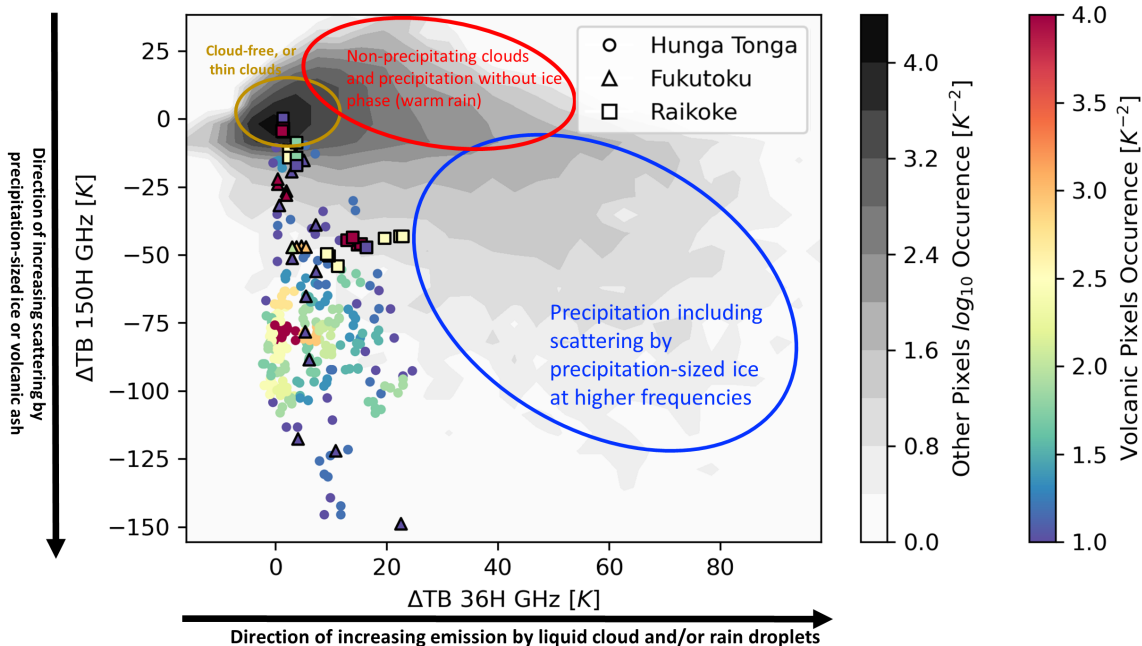
Figure 3.4: Comparison of ΔTB pixel values for a typical atmosphere and volcanic plumes of 150H and 36H GHz. This data is taken from 20 samples of atmospheric states from 2010-2020.

to the previous two eruptions. For HV and FOnB, the 89 frequency range had values of -100 to -200 and -30 to -90 Kelvin, respectively. In contrast, Raikoke had values of 20 to 50 Kelvin. This feature is likely a result of the mixture of emission and scattering from the eruption, as there is a unique mixture of ash and tephra from Raikoke and liquid water from the meteorological clouds. As the frequencies progresses into the upper frequencies (150+), the ΔTB returns to that similar of the previous eruptions, indicating the ascent of ash nucleating into the upper atmosphere.

3.4 Distribution of Pixels

A typical atmosphere contains three regimes of signals as observed by PMW and utilizing ΔTB 36 GHz and 150 GHz, of which is shown in Fig. 3.4. First is the cloud-free or thin cloud region, which is centered in the origin denoted by the gold circle with near zero 36 GHz and 150 GHz ΔTB values. Atmospheric columns that are cloud free or that contain thin cirrus clouds, which are invisible to PMW sensors, will have background levels. Low level clouds that either are non precipitating or precipitating without an ice phase denoted by the red circle have high emission and low scattering, resulting in higher values of ΔTB 36 GHz and near zero ΔTB 150 GHz. Thick clouds that are characterized by regions above the melting layer result in emission by liquid water and scattering by precipitation-sized ice. These clouds are denoted by the blue region and have enhanced levels of ΔTB 36 GHz as well as ΔTB 150 GHz.

For a volcanic eruption, based on our implementation of ΔTB, has a unique atmospheric signature based on the same channels. Pixels from the HV eruption are distributed along the y-axis of Fig. 3.4, with a dense concentration of points near the -75K 150 GHz ΔTB and 0K 36 GHz ΔTB. For FOnB, the pixels are more widely distributed, but there are many pixels along the same region, with -75K to -150K 150 GHz ΔTB and 0K to 23K 36 GHz ΔTB. For the Raikoke eruption, many of the pixels are located near the regions of other meteorological clouds, which we hypothesize is a result of the heavy mixing with the volcanic plume in an atmospheric column. Generally, the volcanic signal occupies a distinct sub-region of this plot as a result of scattering at the higher frequencies but little to no emission at the lower frequencies, which again contrasts to meteorological clouds that have relatively higher emission and scattering effects. Pixels that are nearer to the meteorological clouds are regions closer to the edge of the volcanic plume, which has a lower column density and has reduced scattering effects retrieved by the PMW sensor.

Both FOnB and HV eruptions contain pixels/columns that statistically significant different from other columns in an atmosphere based on Fig. 3.4. Here, FOnB and Raikoke had significantly less pixels as a result of there being less eruption data observed by PMW compared to HV. While the centralized location of the HV eruption pixels are located near 0K 36 GHz and -75 K 150 GHz, many others contain significantly more scattering and are from where the HV eruption was the strongest and ejected the most material high into the atmosphere. Likewise, FOnB had a significant scattering depression in panel d of Fig. 3.2, which resulted in a similar signature of high scattering and low emission.

CHAPTER 4

Conclusion

Here in this study, we present a method for utilizing PMW sensors for the analysis of a subset of recent major eruptions. We hypothesized that volcanic plumes, unlike meteorological clouds, contain a significant amount of scattering from ash/ice coated atmospheric particles while lacking a significant amount of liquid water to produce an emission signal. Employing the conceptual model of ΔTB, or the difference between clear sky simulations and observed values of TB, we focus on differentiating columns/pixels of volcanic plumes and meteorological clouds. Based on the three eruptions studied here, including Hunga Volcano, Fukutoku-Oka-no-Ba, and Raikoke, near zero at low frequencies and large negative values at high frequencies, which contrasts to convective clouds which have large positive values at low frequencies and large negative values at high frequencies. This channel synergy presents a unique signal of volcanic eruptions, which can be disentangled from other columns in the atmosphere. Furthermore, because PMW sensors are insensitive to sufficiently small particles in the atmosphere, there is potential for retrieving features underlying thin ash clouds. We note that there are some limitations to this approach, including the lack of both high spatial and temporal resolutions. This limits our ability to define fine-scale features but are still effective in retrieving large structures and approximate mean values within each pixel. Additionally, we are still able to retrieve multiple overpasses for large eruptions and observe each phase.

While the empirical analysis in this study allows us to isolate the radiative signal of volcanos, it is not sufficient to establish quantitative relations between observed radiative effects and ash properties, such as column ash amount. In future studies, we will therefore extend the use of the RTTOV radiative transfer model to directly simulate the effects of volcanic ash on the brightness temperatures, which will focus on the following:

- **Detectability**: Comparing the visual extent of the ash cloud Fig. 3.1 (g) and (k), we see that PMW observations do not have the same sensitivity to thin ash clouds and/or small ash particles compared to IR observations. Since PMW data is insensitive to small particles, this result is expected. Using radiative transfer simulations of different ash clouds with variable size distributions and thickness, we will be able to determine detectability threshold of ash cloud thickness and particle size for different PMW frequencies as well as different VEI levels of volcanoes.

- **Retrieval of ash column amount**: The three volcanic events plotted in Fig. 3.4 show a dynamic range of 150K at ΔTB of 150 GHz. We postulate that the intensity of the observed scattering signal

is related to a combination of the ash volume amount and ash particle size. As particles get larger and/or ash volume amount increases, the scattering signal becomes larger. The systematic radiative transfer simulations will help understand the nature of the relation between ash scattering signature and ash properties to establish the relation between ash column amount and scattering signature and build simple retrieval algorithms based on those relations. Additionally, the use of different frequencies might be beneficial to determine effective particle size, as different frequencies respond differently to different particle sizes (Bryan et al., 2017).

This would ultimately allow PMW sensors to become a useful tool for the analysis of volcanic eruptions, in which retrieved measurements can be compared to currently utilized satellites.

References

Bennartz, R. and Bauer, P. (2003). Sensitivity of microwave radiances at 85-183 ghz to precipitating ice particles. *Radio Sci*, 38.

Bryan, S., Clarke, A., Vanderkluysen, L., Groppi, C., Paine, S., Bliss, D. W., Aberle, J., and Mauskopf, P. (2017). Measuring water vapor and ash in volcanic eruptions with a millimeter-wave radar/imager. *IEEE Transactions on Geoscience and Remote Sensing*, 55(6):3177–3185.

Carn, S., Clarisse, L., and Prata, A. (2016). Multi-decadal satellite measurements of global volcanic degassing. *Journal of Volcanology and Geothermal Research*, 311:99–134.

Carr, J. L., Horvath, A., Wu, D. L., and Friberg, M. D. (2022). Stereo plume height and motion retrievals for the record-setting hunga tonga-hunga ha'apai eruption of 15 january 2022. *Geophysical Research Letters*, 49:e2022GL098131.

Chen, R. and Bennartz, R. (2020). Sensitivity of 89–190-ghz microwave observations to ice particle scattering. *J Appl Meteorol Clim*, 59:1195–1215.

de Leeuw, J., Schmidt, A., Witham, C. S., Theys, N., Taylor, I. A., Grainger, R. G., Pope, R. J., Haywood, J., Osborne, M., and Kristiansen, N. I. (2021). The 2019 raikoke volcanic eruption – part 1: Dispersion model simulations and satellite retrievals of volcanic sulfur dioxide. *Atmospheric Chemistry and Physics*, 21(14):10851–10879.

Delene, D. J., Rose, W. I., and Grody, N. C. (1996). Remote sensing of volcanic ash clouds using special sensor microwave imager data. *JOURNAL OF GEOPHYSICAL RESEARCH-SOLID EARTH*, 101:11579–11588.

Ekelund, R., Eriksson, P., and Pfreundschuh, S. (2020). Using passive and active observations at microwave and sub-millimetre wavelengths to constrain ice particle models. *Atmospheric Measurement Techniques*, 13(2):501–520.

Fauria, K. E., Jutzeler, M., Mittal, T., Gupta, A. K., Kelly, L. J., Rausch, J., Bennartz, R., Delbridge, B., and Retailleau, L. (2023). Simultaneous creation of a large vapor plume and pumice raft by the 2021 fukutoku-oka-no-ba shallow submarine eruption. *Earth and Planetary Science Letters*, 609:118076.

Grody, N. C., Zhao, L., Ferraro, R. R., Weng, F., and Meng, H. (2008). Determination of precipitable water and cloud liquid water over oceans from the noaa 15 advanced microwave sounding unit. *Journal of Geophysical Research: Atmospheres*, 113(D15).

Gupta, A. K., Bennartz, R., Fauria, K. E., et al. (2022). Eruption chronology of the december 2021 to january 2022 hunga tonga-hunga ha'apai eruption sequence. *Communications Earth & Environment*, 3:314.

Hersbach, H., Bell, B., Berrisford, P., Hirahara, S., Horányi, A., Muñoz Sabater, J., Nicolas, J., Peubey, C., Radu, R., Schepers, D., Simmons, A., Soci, C., Abdalla, S., Abellan, X., Balsamo, G., Bechtold, P., Biavati, G., Bidlot, J., Bonavita, M., and Thépaut, J.-N. (2020). The era5 global reanalysis. *Quarterly Journal of the Royal Meteorological Society*.

Hocking, J., Rayer, P., Rundle, D., and Saunders, R. (2019). RTTOV v12 Users Guide. https://www.nwpsaf.eu/site/software/rttov/documentation/. Accessed: 7 December 2019.

Hou, A. Y., Kakar, R. K., Neeck, S., Azarbarzin, A. A., Kummerow, C. D., Kojima, M., et al. (2014). The global precipitation measurement mission. *Bulletin of the American Meteorological Society*, 95(5):701–722.

Maeno, F., Kaneko, T., Ichihara, M., et al. (2022). Seawater-magma interactions sustained the high column during the 2021 phreatomagmatic eruption of fukutoku-oka-no-ba. *Commun Earth Environ*, 3:260.

Marzano, F. S., Barbieri, S., Vulpiani, G., and Rose, W. I. (2006). Volcanic ash cloud retrieval by ground-based microwave weather radar. *Ieee T Geosci Remote*, 44:3235–3246.

Marzano, F. S. and Coauthors (2018). Multisatellite multisensor observations of a sub-plinian volcanic eruption: The 2015 calbuco explosive event in chile. *Ieee T Geosci Remote*, 56:2597–2612.

Montopoli, M., Cimini, D., Lamantea, M., Herzog, M., Graf, H. F., and Marzano, F. S. (2013). Microwave radiometric remote sensing of volcanic ash clouds from space: Model and data analysis. *Ieee T Geosci Remote*, 51:4678–4691.

Montopoli, M., Vulpiani, G., Cimini, D., Picciotti, E., and Marzano, F. S. (2014). Interpretation of observed microwave signatures from ground dual polarization radar and space multi-frequency radiometer for the 2011 grimsvotn volcanic eruption. *ATMOSPHERIC MEASUREMENT TECHNIQUES*, 7:537–552.

National Center for Atmospheric Research Staff (2022). The climate data guide: Hoaps: Hamburg ocean atmosphere parameters and fluxes from satellite data. https://climatedataguide.ucar.edu/climate-data/hoaps-hamburg-ocean-atmosphere-parameters-and-fluxes-satellite-data. Last modified 2022-09-09.

Petty, G. W. (1994a). Physical retrievals of over-ocean rain rate from multichannel microwave imagery. part i: Theoretical characteristics of normalized polarization and scattering indices. *Meteorology and Atmospheric Physics*, 54(1-4):79–99.

Petty, G. W. (1994b). Physical retrievals of over-ocean rain rate from multichannel microwave imagery. part ii: Algorithm implementation. *Meteorol. Atmos. Phys.*, 54:101–121.

Petty, G. W. (2006). *A first course in atmospheric radiation*.

Prata, F. and Lynch, M. (2019). Passive earth observations of volcanic clouds in the atmosphere. *Atmosphere*, 10.

Robock, A. (2001). *Volcanic eruptions and climate change*, pages 191–219.

Romeo, F., Mereu, L., Scollo, S., Papa, M., Corradini, S., Merucci, L., and Marzano, F. S. (2023). Volcanic cloud detection and retrieval using satellite multisensor observations. *REMOTE SENSING*, 15.

Saunders, R. and Coauthors (2007). A comparison of radiative transfer models for simulating atmospheric infrared sounder (airs) radiances. *J. Geophys. Res.*, 112:D01S90.

Saunders, R. and Coauthors (2018). An update on the rttov fast radiative transfer model (currently at version 12). *Geosci. Model Dev.*, 11:2717–2737.

Skofronick-Jackson, G. and Johnson, B. T. (2002). Surface and atmospheric contributions to passive microwave brightness temperatures for falling snow events. *Journal of Applied Meteorology*, 41(3):240–255.

Wen, S. and Rose, W. I. (1994). Retrieval of sizes and total masses of particles in volcanic clouds using avhrr bands 4 and 5. *Journal of Geophysical Research*, 99(D3):5421.

Wilson, T. M., Stewart, C., Sword-Daniels, V., Leonard, G. S., Johnston, D. M., Cole, J. W., Wardman, J., Wilson, G., and Barnard, S. T. (2012). Volcanic ash impacts on critical infrastructure. *Physics and Chemistry of the Earth, Parts A/B/C*, 45-46:5–23. Volcanic ash: an agent in Earth systems.

Wright, C., Hindley, N., Alexander, M., et al. (2022). Surface-to-space atmospheric waves from hunga tonga–hunga ha'apai eruption. *Nature*, 609:741–746.